International Journal of Pharmaceutics 605 (2021) 120790

Contents lists available at ScienceDirect

International Journal of Pharmaceutics

journal homepage: www.elsevier.com/locate/ijpharm

Multicomponent ionic crystals of diltiazem with dicarboxylic acids toward understanding the structural aspects driving the drug-release

Luan F. Diniz [a,b], Chris H.J. Franco [c,d], Daniely F. Silva [b], Larissa S. Martins [b], Paulo S. Carvalho Jr [e], Mateus A.C. Souza [a], Naialy F.A. Reis [a], Christian Fernandes [a], Renata Diniz [b,*]

[a] Laboratório de Controle de Qualidade de Medicamentos e Cosméticos, Departamento de Produtos Farmacêuticos, Faculdade de Farmácia, Universidade Federal de Minas Gerais, 31270-901 Belo Horizonte, MG, Brazil
[b] Departamento de Química, Instituto de Ciências Exatas (ICEx), Universidade Federal de Minas Gerais, 31270-901-Belo Horizonte, MG, Brazil
[c] Departamento de Química, Instituto de Ciências Exatas (ICE), Universidade Federal de Juiz de Fora, 36036-900-Juiz de Fora, MG, Brazil
[d] Instituto Superior Técnico, Universidade de Lisboa, Av. Rovisco Pais, 1049-001 Lisboa, Portugal
[e] Instituto de Física, Universidade Federal do Mato Grosso do Sul, 79074-460 Campo Grande, MS, Brazil

ARTICLE INFO

Keywords:
Diltiazem
Salt
Cocrystal
X-ray diffraction
Solubility
Dissolution

ABSTRACT

Diltiazem (DIL) is a calcium channel blocker antihypertensive drug commonly used in the treatment of cardiovascular disorders. Due to the high solubility and prompt dissolution of the commercial form hydrochloride (DIL-HCl) that is closely related to short elimination drug half-life, this API is known for exhibiting an unfitted pharmacokinetic profile. In an attempt to understand how engineered multicomponent ionic crystals of DIL with dicarboxylic acids can minimize these undesirable biopharmaceutical attributes, herein, we have focused on the development of less soluble and slower dissolving salt/cocrystal forms. By the traditional solvent evaporation method, two hydrated salts of DIL with succinic and oxalic acids (DIL-SUC-H_2O and DIL-OXA-H_2O), and one salt-cocrystal with fumaric acid (DIL-FUM-H_2FUM) were successfully prepared. An in-depth crystallographic description of these new solid forms was conducted through single and powder X-ray diffraction (SCXRD, PXRD), Hirshfeld surface (HS) analysis, energy framework (EF) calculations, Fourier Transform Infrared (FT-IR) spectroscopy, and thermal analysis (TG, DSC, and HSM). Structurally, the inclusion of dicarboxylic acids in the crystal structures provided the formation of 2D-sheet assemblies, where ionic pairs (DIL^+/$anion^-$) are associated with each other *via* H-bonding. Consequently, a substantial lowering in both solubility (16.5-fold) and intrinsic dissolution rate (13.7-fold) of the API has been achieved compared to that of the hydrochloride salt. These findings demonstrate the enormous potential of these solid forms in preparing of novel modified-release pharmaceutical formulations of DIL.

1. Introduction

The development of multicomponent solid forms, *e.g.*, salts, cocrystals, and its other derived crystal forms, from known active pharmaceutical ingredients (APIs), is often guided by the crystal engineering (CE) principles (Berry and Steed, 2017; Blagden et al., 2007; Schultheiss and Newman, 2009). CE states that it is possible to design new solids with optimized physicochemical properties since the intermolecular interactions in the context of crystal packing are understood (Desiraju, 2013). Among the remarkable CE contributions that have even provided unprecedented advances in pharmaceutical routines (Duggirala et al., 2016; Shan and Zaworotko, 2008), the major one is the ability to design novel crystal arrangements. In this case, a complementary molecule (coformer) is included without making or breaking covalent bonds, hence, preserving the drug pharmacological activities while its physicochemical properties (aqueous solubility, dissolution rate, permeability, and hygroscopicity) can be improved (Elder et al., 2013; Serajuddin, 2007; Steed, 2013). Within this framework, salt and cocrystal formation has gained enormous attention not only for its technological (Karimi-Jafari et al., 2018) and legal (Gadade and Pekamwar, 2016) importance but also for allowing the screening and selection of the most suitable solid form of a particular API. Accordingly, the choice

* Corresponding author.
E-mail address: dinizr@qui.ufmg.br (R. Diniz).

https://doi.org/10.1016/j.ijpharm.2021.120790
Received 12 February 2021; Received in revised form 4 June 2021; Accepted 6 June 2021
Available online 8 June 2021

for pharmaceutically acceptable coformers is now an essential part of the drug product development process to overcome common pharmaceutical issues of APIs.

Diltiazem (DIL, Scheme 1) is a benzothiazepine derivative calcium antagonist drug used to treat hypertension, angina, and certain heart rhythm disorders (Weir, 1995). It is formulated using the active enantiomer (*S*)-diltiazem in the form of a hydrochloride salt (DIL-HCl). This form is freely soluble in water (565 mg mL^{-1}) (Han et al., 2013) and also known for exhibiting a short elimination drug half-life (3.2 ± 1.3 h) (Hermann et al., 1983), requiring administration of immediate-release 30 mg tablets from three to four times daily. To compensate for such unfavorable features associated with DIL, extended-release capsules containing 120–240 mg of drug and administered once daily are commercially available. However, even in these slow-release preparations, the choice for a crystal form of DIL with lower solubility and with a slower dissolution rate would be preferable over hydrochloride salt. Furthermore, diverse alternative approaches have also been employed to minimize the DIL issues, which include Eudragit-coated microparticles (Kristmundsdóttir et al., 1996), liquisolid tablets (Kaialy et al., 2016), polymeric matrices systems (Kojima et al., 2008), and microencapsulation (Farhana et al., 2009). Despite the use of all these technologies, none of them have been able to overcome the DIL problems thoroughly.

Over the last years, crystal engineering technology was quite employed to improve the API's solubility (Blagden et al., 2007; Elder et al., 2013; Serajuddin, 2007). The ability of multicomponent solid forms in tuning drug-releasing profile, although it is not a trivial task, is featured as the state of art and one of the innovation pillars in the crystal engineering field. Nevertheless, very few studies published so far have been able to establish how engineered supramolecular architectures would promote a suitable API-releasing from modified crystal arrangements (Almansa et al., 2017; Cheney et al., 2010; Gascon et al., 2019). Based on the cocrystallization strategy, only one published study involving DIL has been investigated to date. Although Stepanovs *et al.* (Stepanovs et al., 2016) have described three salts, it remains unclear how novel DIL solid forms could modulate the drug-releasing since only by comparative crystal structures analyzes, would be reckless to reach that conclusion. Additionally, even though the salts reported have demonstrated reductions in DIL solubility, their dissolution behaviors have not been accessed, becoming any prediction on the impact on the absorption process and, consequently, on the elimination drug half-life at least questionable. Thus, a comprehensive investigation, in biopharmaceutical and solid-state terms, to assist in the understanding of which structural and energy framework aspects govern both solubility and dissolution processes of this API remains highly demanded.

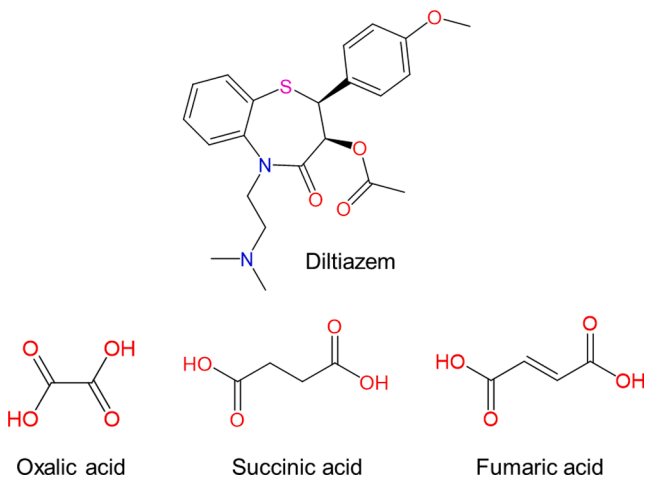

Scheme 1. Molecular structure of DIL and dicarboxylic acids (coformers) used in this study.

Given this scenario, in the present investigation, aiming to establish the structural attributes that exert more influence on both solubility and dissolution rate of DIL from planned crystal arrangements, we report a protocol for the supramolecular synthesis of two hydrated salts (DIL-SUC-H_2O and DIL-OXA-H_2O) obtained from the reactions of DIL with succinic and oxalic acids and also an anhydrous salt-cocrystal (DIL-FUM-H_2FUM) obtained from the reaction between DIL and fumaric acid (see Scheme 1). Besides a thorough solid-state characterization by single-crystal and powder X-ray Diffraction (SCXRD, PXRD), Hirshfeld surface analysis (HS) and energy framework (EF) calculations, Fourier-transform Infrared (FT-IR) spectroscopy, thermogravimetry (TG), differential scanning calorimetry (DSC), and hot-stage microscopy (HSM), we also performed equilibrium solubility as well as dissolution studies. All these analyzes certainly introduce valuable insights concerning the pharmacological use of DIL since their novelty multicomponent crystals proved to be pharmaceutically advantageous over commercial salt DIL-HCl.

2. Material and methods

2.1. Materials

Enantiomerically pure (*S*)-diltiazem hydrochloride (DIL-HCl) and organic solvents (chromatographic grade) was obtained from local suppliers and used without any further purification. Succinic, oxalic and fumaric acids were purchased from Sigma-Aldrich Brazil® and used as received. Ultrapure water was obtained from a Millipore Direct Q3 system and used directly.

2.2. Preparation of DIL salts and crystallization

Diltiazem free base (DIL) has been prepared from the hydrochloride salt. Two grams of DIL-HCl (4.434 mmol) were dissolved in 50 mL of ultrapure water followed by the addition of 0.98 g of Na_2CO_3 (11.665 mmol). This mixture was stirred for ~20 min and the white product formed as precipitated, corresponding to DIL free base (see Figure S1) and with a yield above 85%, was filtered and further dried within desiccator at room temperature, before being used in the salt's preparation. All new crystal forms derived from DIL were prepared following the same protocols.

Diltiazem succinate monohydrate (*DIL-SUC-H_2O*) – 50 mg (0.121 mmol) of DIL free base were weighed and dissolved in 5 mL of acetonitrile/water (2:1, v/v) solution. Then, 14.5 mg (0.121 mmol) of succinic acid was added, followed by the system stirring at 70 °C for 20 min. Colorless plate crystals were obtained within 4–5 days, with a yield of ~90%, upon slow solvent evaporation at room temperature.

Diltiazem oxalate dihydrate (*DIL-OXA-H_2O*) – 50 mg (0.121 mmol) of DIL free base and 10.8 mg (0.121 mmol) of oxalic acid were dissolved in 5 mL of methanol/water (2:1, v/v) solution. This mixture was stirred under ambient conditions for 15 min. Colorless prism crystals were obtained in 5 days, with yield above 85%, by slow evaporation of solvent at room temperature. Attempts to obtain better quality single-crystals of this salt using any other crystallization techniques have not been successful.

Diltiazem fumarate-fumaric acid (*DIL-FUM-H_2FUM*) – 50 mg (0.121 mmol) of DIL free base and 14.0 mg (0.121 mmol) of fumaric acid were dissolved in 5 mL of ethanol/acetonitrile (1:1, v/v) solution under stirring at 80 °C for 20 min. The system was left for slow evaporation of solvent at room temperature and colorless prismatic crystals appeared in 6 days, with a crystallization yield of ~92%.

2.3. X-ray diffraction analysis

Single crystal X-ray diffraction data were collected at room temperature in an Agilent-Rigaku Super Nova diffractometer with AtlasS2 CCD detector system equipped with both Mo (λ = 0.71073 Å) and Cu (λ

= 1.5418 Å) microfocus radiation sources. The CrysAlisPro (Rigaku Oxford Diffraction, 2014) data reduction package was used for indexing, integration, and unit cell determination. Thereafter, using Olex2 (Dolomanov et al., 2009), the structures were solved by direct methods (SHELXT-14) (Sheldrick, 2015a) and refined by full-matrix least-squares on F^2 (SHELXL-17) (Sheldrick, 2015b). All non-hydrogen atoms were refined anisotropically. Hydrogen atoms were located from electron-density difference maps and were positioned geometrically and refined according to the riding model [$U_{iso}(H) = 1.2U_{eq}$ or $1.5U_{eq}$]. MERCURY 4.3.1 (Macrae et al., 2020), ToposPro (Blatov et al., 2014), CrystalExplorer17 (Turner et al., 2017) and ORTEP3 for Windows (Farrugia, 2012) programs were used to prepare the graphical representations for publication. All deposited *CIF* files are in the Cambridge Structural Database (Groom et al., 2016) under the CCDC numbers 2058965, 2058966, 2058967 and 2059068.

Powder X-ray diffraction data were acquired at room temperature using a Bruker D8 Advance DaVinci diffractometer, in a Bragg-Brentano geometry, under 40 kV of voltage and 40 mA of current and using CuKα radiation (λ = 1.5406 Å), Ni filter and LynxEye Detector. The diffractograms were acquired over an angular range of 3−50° (2θ) with a step size of 0.01° (2θ) and a constant counting time of 5 s per step.

2.4. Hirshfeld surface analysis and energy framework calculations

Hirshfeld surface (HS) analysis and energy framework (EF) calculations have been performed on CrystalExplorer17 software (Turner et al., 2017) using the *CIF* files as input. The Hirshfeld surfaces and their associated 2D-fingerprint plots were generated to further investigate the contribution of the various intermolecular contacts toward understanding the distinct DIL crystal packings. Each HS was generated using the normalized contact distances (d_{norm}) that are defined in terms of d_i (distance to the nearest nucleus within the surface) and d_e (distance from the point to the nearest nucleus external to the surface) relative to the van der Waals radii of the atoms (Spackman and Jayatilaka, 2009). The d_{norm} surfaces were mapped over the color scale, ranging from blue (longer than van der Waals contact), white (contacts with a length close to the van der Waals sum), and red (shorter than van der Waals contact).

The energy frameworks were computed based on B3LYP/6-31G (d,p) molecular wavefunctions calculated at the crystal geometry to obtain a quantitative insight into the intermolecular interaction energy in the crystalline environment and also to visualize the energy topologies (Turner et al., 2015) displayed by a cluster of molecules in the novel DIL crystal structures. The total intermolecular interaction energy (E_{tot}) is given as the sum of the electrostatic (E_{ele}), polarization (E_{pol}), dispersion (E_{dis}), and exchange–repulsion (E_{rep}) components, with scale factors of 1.057, 0.740, 0.871 and, 0.618, respectively (Mackenzie et al., 2017). Intermolecular interactions between two adjacent molecules were ignored when the closest interatomic distance was higher than 3.8 Å. The resulting energy frameworks were graphed by connecting the centers of mass of molecules so that the cylinder thicknesses are set in proportion to the magnitude of the intermolecular interaction energies.

2.5. Fourier transformed Infrared spectroscopy

Fourier Transform Infrared (FT-IR) spectra were recorded on a Perkin-Elmer Spectrum One spectrometer fitted with an ATR reflectance attachment in the range of 4000–650 cm^{-1}, with an average of 64 scans and spectral resolution of 4 cm^{-1}.

2.6. Thermal analysis

Differential Scanning Calorimetry (DSC) curves were obtained on a Shimadzu DSC-60 instrument. The samples (1.0 ± 0.2 mg) were placed in sealed aluminum pans and heated at a constant rate of 10 °C min^{-1} under N_2 flow (50 mL min^{-1}) from 25 °C until the degradation temperature of each compound. Thermogravimetric (TG) experiments were carried out on a Shimadzu DTG-60 thermobalance. Approximately 2.0 mg of each sample was placed in alumina pans and heated at 10 °C min^{-1} under a nitrogen flow (50 mL min^{-1}) from 25 to 600 °C. All thermal analysis data were analyzed by the Shimadzu TA-60 software. Hot-Stage Microscopy (HSM) examinations were performed using a Leica DM2500P optical microscope connected to a Linkam T95-PE hot-stage equipment. The single-crystals were heated at a ramp rate of 10 °C min^{-1} until the beginning of the melting. Both heating and acquisition of the photomicrographs were controlled *via* Lynksys 32 software.

2.7. High performance liquid chromatography conditions

The concentrations of DIL in solutions from solubility and dissolution studies were determined in a Waters Alliance HPLC system composed of an e2695 separation module, a column oven, and a 2489 UV–VIS detector. Empower 3.0 software was used for both data acquisition and analysis. The separation was conducted at 30 °C using an Agela Technologies Innoval C18 (150 mm × 4.6 mm i.d., 5.0 μm particle size) column. The mobile phase consisted of a mixture of a 0.05% (v/v) trifluoroacetic acid aqueous solution and a 0.05% (v/v) trifluoroacetic acid methanolic solution (44:56, v/v), delivered at a flow rate of 1.0 mL min^{-1}. DIL was detected at 240 nm and the injection volume was 20 μL. The validation of this method has been performed according to ICH Q2 (R1) guideline - Validation of analytical procedures: text and methodology (ICH, 2005). The parameters selectivity, linearity, precision, and accuracy were evaluated. The main results of the validation study are summarized in Table S1.

2.8. Solubility and dissolution studies

The salts solubilities were determined by the shake-flask method (Glomme et al., 2005) at 37 °C in buffered aqueous media with pH ranging from 1.2 to 6.8. Suspensions were prepared, in triplicate, stirring an excess amount of the samples, sufficient to reach saturation, into 2 mL of each dissolution media for a period of 24 h. Then, the suspensions were filtered through a 0.45 μm PVDF syringe filter and diluted in their respective dissolution media before being quantified by HPLC. After the equilibrium solubility experiments, the pH value in each dissolution medium was measured by a pH meter and the remaining solid residues were analyzed by FT-IR to identify their solid-state form.

Intrinsic dissolution rate (IDR) measurements were performed on a rotating disk dissolution apparatus. For IDR experiments, a defined quantity of each sample, *i.e.*, 200 mg (new DIL salts) and 300 mg (DIL-HCl) has been compressed by a hydraulic press at 1 kN for 1 min to form nonporous and compact 0.5 cm^2 disks with a flat surface on one side. The intrinsic attachment with the sample was rotated at 100 rpm in 900 mL of purified water medium (pH ~ 5.9) preheated at 37 ± 0.5 °C. At specific time intervals (2, 3, 4, 5, 7, 10, 15 min), 5 mL of dissolution medium was withdrawn (with volume replacement) and immediately filtered through 0.45 μm PVDF syringe filter before the concentration of dissolved DIL being measured by HPLC. Any possible phase transitions during the IDR experiments and/or disk compression were monitored by FT-IR from the undissolved solids.

Finally, the dissolution profiles of capsules containing a quantity of diltiazem-related salts equivalent to 30 mg of DIL, and the excipients lactose and cellulose were obtained using a Hanson SR8-Plus dissolution test station. Purified water (900 mL, pH ~ 5.9), maintained at 37.0 ± 0.5 °C, was employed as the dissolution medium and stirred at 75 rpm using USP apparatus 2 (paddles). At the same time intervals of the IDR measurements, aliquots of 5.0 mL were withdrawn (with volume replacement), diluted if necessary, and quantified by HPLC. All dissolution measurements were carried out in triplicate. The salts were previously milled and sieved (75–150 μm) before being encapsulated to minimize the size effect of the crystals on dissolution performance.

3. Result and discussion

A decrease in DIL solubility can be achieved by multicomponent ionic crystals that exhibit structures with the prevalence of hydrophobic domains over the hydrophilic ones and thereby with less accessibility to water molecules during the dissolution. Thus, the salt/cocrystal formation strategy with dicarboxylic acids assembling ionic molecules into a more cohesive structure (compared to the DIL-HCl) through the stabilizing charge-assisted hydrogen bonds (CAHBs) allows reaching this demand. DIL free base contains an ionizable tertiary amine group ($pK_a = 7.7$) on the *dimethylaminoethyl* fragment liable to be protonated at acid medium, providing salt formation. The estimated pK_a difference (ΔpK_a) between the DIL and selected coformers suggests salt formation since ΔpK_a of the reactions is superior to 3 units (see Table S2) (Childs et al., 2007; Cruz-Cabeza, 2012). By the partial deprotonation of dicarboxylic acids, the DIL molecule becomes ionized to form novel supramolecular architectures through the $N^+-H\cdots O^-$ H-bonds (Li et al., 2018). The additional *COOH* group can play a key role in the ionic pairs (DIL^+/$anion^-$) assembly. All of these assumptions were supported by a thorough survey of all DIL structures and analogues reported in the Cambridge Structural Database (CSD) (Groom et al., 2016). This survey also revealed that succinic, oxalic, and fumaric dicarboxylic acids are the most suitable coformers to the co-crystallization experiments with DIL.

3.1. Crystallographic description

Herein, three ionic multicomponent systems of DIL have been supramolecularly synthesized: two hydrated salts with succinic and oxalic acids (DIL-SUC-H_2O and DIL-OXA-H_2O, respectively) and an anhydrous salt-cocrystal with fumaric acid (DIL-FUM-H_2FUM). In all cases, the corresponding crystals have been prepared according to the traditional solvent evaporative method (see Section 2.2). The asymmetric unit (ASU) of DIL salts is depicted in Figure S2 and Table 1 summarizes the crystallographic and refinement data. Overall, in the three solid forms, the coformers exhibit disorder effects due to their distinct crystalline packing positions. The disorder refined displays occupational values of 0.78:0.22, 0.59:0.41, and 0.65:0.35 for succinic, oxalic, and fumaric acids, respectively. For DIL-OXA-H_2O in particular, the high-disorder effect in the crystal structure hampered hydrogen atoms localization derived from the water and oxalate molecules. Concerning the absolute configuration at the chiral centers, all DIL salts display an *S*-type configuration and, hence, they are found to be enantiomerically pure forms. This observation agrees with the Flack parameter values (Flack and Bernardinelli, 1999) found by refining the structures (see Table 1).

Since no significant geometric differences are expected for N2-atom after protonation, the formation of salts has been firstly demonstrated by the identification of COO^- groups on the anion structures, resulting from the proton transfer of each dicarboxylic acid to the DIL molecule. The resonant character of the C–O bond in the carboxylate group is evidenced by a short difference in the C–O values (ΔD_{C-O}). The DIL-SUC-H_2O salt is formed by the partial protonation of the acid molecule having ΔD_{C-O} values of 0.048 and 0.059 Å for its *COOH* groups in the anion. Due to the poor quality of DIL-OXA-H_2O crystals, the oxalate anion chemical nature has been additionally characterized through vibrational spectroscopy analysis (see section 3.3.2). The DIL-FUM-H_2FUM salt-cocrystal results from a complex ionic balance because its structure comprises a neutral fumaric acid molecule with ΔD_{C-O} values of 0.095 and 0.106 Å for the *COOH* groups and a fully ionized (deprotonated) anion having ΔD_{C-O} values of 0.023 and 0.062 Å for the COO^- groups.

From a conformational point of view, the DIL^+ cation has distinct molecular conformations. The superpositions of DIL^+ cation molecules derived from the three salts, highlighting the conformational differences between them are shown in Figures S3 and S4. It is noticed that the *benzothiazepine* ring displays a slightly twisted-boat configuration with the absolute conformation of M−type, similar to that described by Kojić-Prodić *et. al.* (Kojić-Prodić et al., 1984). The *dimethylaminoethyl* fragment demonstrated to be the most flexible moiety of DIL^+ cations. While the torsion angle C4–N1–C19–C20 is 115.2(7)° in the DIL-SUC-H_2O salt and 107.5(7)° in the DIL-OXA-H_2O salt, the same torsion angle is −90.95(5)° and −53.73(1)° in the DIL-FUM-H_2FUM salt-cocrystal. Indeed, these variations are likely related to the different intermolecular forces induced by the combination of the DIL drug and the dicarboxylic acids. Finally, a detailed evaluation of each crystal structure and its packing is provided below, and the geometric parameters of the H-bonds are listed in Table 2.

Table 1
Crystallographic parameters and refinement details of DIL-HCl and its new derived salt forms.

Identification code	DIL-HCl*	DIL-SUC-H_2O	DIL-OXA-H_2O	DIL-FUM-H_2FUM
Chemical formula	$C_{22}H_{27}ClN_2O_4S$	$C_{26}H_{34}N_2O_9S$	$C_{24}H_{27}N_2O_8S$	$C_{52}H_{60}N_4O_{16}S_2$
Molecular weight	450.96	550.61	504.15	1061.16
Temperature (K)	293(2)	293(2)	293(2)	293(2)
Crystal system	Orthorhombic	Monoclinic	Monoclinic	Monoclinic
Space group	$P2_12_12_1$	$P2_1$	$C2$	$P2_1$
a (Å)	6.0368(2)	8.8575(9)	47.881(4)	9.0217(6)
b (Å)	9.0741(3)	6.6437(6)	6.1551(4)	24. 7529(14)
c (Å)	42.1870(12)	25.0886(19)	8.8416(4)	11.9962(9)
α (°)	90	90	90	90
β (°)	90	97.690(9)	95.229(5)	93.759(6)
γ (°)	90	90	90	90
Volume (Å)^3	2310.94(13)	1463.1(2)	2594.9(3)	2673.1(3)
Z / Z'	4 / 1	2 / 1	4 / 1	2 / 2
ρ_{calc} (g cm^3)	1.296	1.246	1.291	1.318
μ (mm^{-1})	2.556	0.162	1.530	0.172
Radiation type	Cu Kα	Mo *K*α	Cu Kα	Mo *K*α
2θ range for data collection/°	9.97 to 136.42	4.916 to 50.74	3.71 to 136.27	4.814 to 50.75
Reflections collected	19,135	13,695	14,842	15,785
Independent reflections	4186	5210	3992	9186
Unique reflections	3591	3964	3567	7074
R_1 [$I \geq 2\sigma(I)$]	0.0400	0.0639	0.0967	0.0524
wR_2 [all data]	0.0997	0.1874	0.2611	0.1334
Goodness-of-fit on F^2	1.055	1.043	1.127	1.052
Flack parameter	−0.028(12)	−0.01(5)	−0.04(4)	−0.03(4)

* *redetermination*

Table 2
Selected geometric parameters of the H-bonds in the new DIL salt forms.

Interaction	D···A(Å)	D − H···A(°)	Symmetry Code
DIL-SUC-H_2O			
Ow−HwA···O5	2.707(7)	168	2-x,1/2 + y,1-z
N2−H2···O5	2.604(7)	173	2-x,1/2 + y,1-z
N2−H2···O6	3.103(7)	124	2-x,1/2 + y,1-z
Ow−HwB···O6	2.634(7)	173	2-x, y-1/2,1-z
O7−H7A···Ow	2.566(7)	166	2-x, y-1/2,1-z
C18−H18A···O4	3.311(10)	143	x,y + 1,z
C18−H18C···O1	3.259(9)	148	-x,1/2 + y,-z
C19−H19B···O3	3.489(9)	171	x,y-1,z
C21−H21B···O7	3.171(8)	129	x-1,y,z
C22−H22B···O8	3.297(11)	153	1-x, y-1/2,1-z
C22−H22C···O3	3.172(9)	126	x,y-1,z
DIL-OXA-H_2O			
N2−H2···O5	2.940(3)	144	x,y,z
N2−H2···O7	2.865(18)	135	x,y,z
C7−H7···O3	3.398(10)	148	x,-1 + y,z
C18−H18A···O4	3.120(8)	130	x,1 + y,z
C18−H18C···O1	3.290(9)	157	x,y,-1 + z
C19−H19B···O3	3.334(9)	175	3/2-x,-1/2 + y,2-z
C22−H22B···O8	3.340(3)	143	1-x,y,1-z
DIL-FUM-H_2FUM			
N2A−H2A···O1	2.815(7)	145	x,y,z
N2A−H2A···O2	2.989(6)	144	x,y,z
N2B−H2B···O3	2.787(8)	149	x,y,z
N2B−H2B···O4	3.020(7)	147	x,y,z
O5−H5···O4	2.468(8)	143	x,y,z
O7−H7···O2	2.495(7)	155	x,y,z + 1
C7A−H7A···O4A	3.309(7)	136	x + 1,y,z
C7B−H7B···O4B	3.291(7)	135	x-1,y,z
C15A−H15A···O4A	3.247(7)	137	x-1,y,z
C15B−H15B···O4B	3.166(7)	139	x-1,y,z
C21A−H21C···O8	3.398(11)	155	x + 1,y,z-1
C21B−H21E···O1	3.370(9)	148	x-1,y,z
C22A−H22A···O7	3.415(11)	145	x + 1,y,z-1
C22A−H22C···O3	3.284(12)	143	x + 1,y,z
C22B−H22D···O6	3.440(9)	169	x-1,y,z
C22B−H22F···O8	3.382(9)	158	x-1,y,z
C24A−H24A···O7	3.210(13)	129	x,y,z-1
C25A−H25A···O5	3.149(13)	127	x,y,z-1
C28−H28···O4	3.084(10)	130	x,y,z-1
C29−H29···O2	3.070(9)	129	x,y,z + 1

3.1.1. Diltiazem succinate monohydrated (DIL-SUC-H_2O)

DIL-SUC-H_2O crystallizes as a 1:1 monohydrated molecular salt in the monoclinic $P2_1$ space group with Z' = 1. As shown in Figure S2a, the ASU has a DIL^+ cation, protonated on the amino tertiary group, a hydrogen-succinate anion ($HSUC^-$), and a water molecule. In the DIL-SUC-H_2O salt structure, the protonated N2-atom of tetrahedral geometry on the DIL^+ cation is connected with $HSUC^-$ anion *via* $N2^+$−H2···$O5^-$ (*d*: 2.604(7) Å; θ: 173°) and $N2^+$−H2···$O6^-$ (*d*: 3.103(7) Å; θ: 124°) CAHBs. Also, through the O7−H7A···Ow (*d*: 2.566(7) Å; θ: 166°) H-bond, the *COOH* group of $HSUC^-$ anion is associated with a water molecule (Fig. 1a), resulting in the formation of a discrete chain with $D_1^1(2)[*, a, b, c, d]$ topology (Grell et al., 1999; Motherwell et al., 2000). Two other classical Ow−HwA···$O5^-$ (*d*: 2.707(7) Å; θ: 168°) and Ow−HwB···$O6^-$ (*d*: 2.634(7) Å; θ: 173°) H-bonds, named *c* and *d*, connect different water molecules to each COO^- group from $HSUC^-$ anion and, when combined with the type-*b* H-bond, extend the crystal structure along the *b*-axis, hence building an infinite double 1D-chain, which connects each other by C–H···O (see Table 2) interactions, building a sheet (Fig. 1b). No π-π interaction is observed between aromatic groups of adjacent DIL^+ cations and the double-chains interact with each other in *ac*-plane to complete the three-dimensional packing (Fig. 1c). To systematize crystal packing trends, a topological analysis has been applied to DIL salts. For the topological description of H-bonds, we considered the main intermolecular contacts and, for the construction of the simplified model for the crystal network, the molecules/cations/anions were considered as a vertex, with the actual connection of the H-bonds as an edge (see Figure S5). For DIL-SUC-H_2O, the topological description reveals that the supramolecular assemblies are characterized by an infinite double 1D-chain, connected by weak C–H···O non-classical H-bonds (Table 2). The system shows a topological description featured as a bi-dimensional 3-nodal net with the following point symbol $(4^2.6^3.8)(4^2.6)(6^3)$ and ***3,3,4L6*** topological type.

3.1.2. Diltiazem oxalate dihydrate (DIL-OXA-H_2O)

DIL-OXA-H_2O salt featured as prismatic crystals of poor quality, *i.e.,* their diffraction pattern did not extend to a high resolution, which imposed several difficulties during the crystal structure determination. Despite the disorder on both oxalate anion and water molecules, which did not allow the inclusion of the H-atoms, the final model refined has yielded adequate refinement indicators (see Table 1). DIL-OXA-H_2O is a 1:1 dihydrated molecular salt that crystallizes in the monoclinic crystal system with *C*2 space group and Z' = 1. The ASU (Figure S2b) comprises one DIL^+ cation, one disordered hydrogen-oxalate anion ($HOXA^-$, see section 3.3.2), and two disordered water molecules. In the salt structure, DIL^+ cation has the protonated amine group towards to mean plane of $HOXA^-$ anion, forming an ionic pair that is stabilized by the bifurcated $N2^+$−H2···$O7^-$ (*d*: 2.865(18) Å; θ: 135°) and $N2^+$−H2···$O5'^-$ (*d*: 2.940(3) Å; θ: 144°) CAHBs (Fig. 2a). Although the H-atoms assignment of water molecules was not possible from the electronic density maps, the $\langle O_w \cdots O_{anions}$ distance of 2.470 Å indicates the formation of an anion···water system. Similar to DIL-SUC-H_2O salt, the DIL-OXA-H_2O crystal packing also presents a columnar arrangement. Ionic pairs are linked to each other by C−H···O (Table 2) H-bonds such that the DIL^+ cations and the anion···water system are alternately arranged in a 1D-chain along [0 0 1] direction. The anion···water system is responsible to held chains together, forming a sheet structure (Fig. 2c). A 3D-network structure is formed by stacking of sheets that are further stabilized by C16−H16C···π (*d*: 3.547(2) Å) interactions (Fig. 2b) between the aromatic rings of DIL^+ cations. Structurally, the main H-bonds formed in DIL-OXA-H_2O has $D_1^1(2)[a]$ topology. The C–H···O interactions from *phenyl*- and *acetate*-fragments of DIL^+ cations have been considered and then, it is possible to verify the formation of 2D-sheets along the *ac*-plane with the water molecules accommodated between these. These considerations show the formation of a two-dimensional ***2,4L1*** type network (2,4)-connected with $(\mathbf{4.8^5})$**. 4** point symbol (Figure S6).

3.1.3. Diltiazem fumarate-fumaric acid (DIL-FUM-H_2FUM)

DIL-FUM-H_2FUM belongs to the monoclinic $P2_1$ space group with Z' = 2. Its structure is a salt-cocrystal (Grothe et al., 2016) comprising two independent DIL^+ cations (A and B), a fumarate anion (FUM^{2-}), and a neutral fumaric acid (H_2FUM) in the ASU (Figure S2c). Thus, the DIL-FUM-H_2FUM has a 2:1:1 stoichiometry for cation:anion:neutral acid. The crystal structure analysis revealed that both DIL^+ A and B cations are connected to the FUM^{2-} anion through bifurcated N–H···O CAHBs ($N2A^+$−H2A···$O1^-$, *d*: 2.815(7) Å; θ: 145° and $N2A^+$−H2A···$O2^-$, *d*: 2.989(6) Å; θ: 144° / $N2B^+$−H2B···$O3^-$, *d*: 2.787(8) Å; θ: 149° and $N2B^+$−H2B···$O4^-$, *d*: 3.020(7) Å; θ: 147°), as depicted in Fig. 3a. The H_2FUM molecules bridge FUM^{2-} anions *via* O5−H5···O4 (*d*: 2.468(8) Å; θ: 143°) H-bonds to form a 1D chain along the [0 0 1] direction in which DIL^+ cations are attached (Fig. 3b). As result, the assembly of these units generates a 3D-network arrangement as shown in Fig. 3c. The interactions set involving the COO^- groups of the FUM^{2-} anion form a discrete chain with $D_1^1(2)[a, b, c, d]$ topology (Fig. 3a), similar to that one found for DIL-SUC-H_2O salt. Furthermore, an infinite chain $C_2^2(14)[e, f]$ topology formed between FUM^{2-} anions and H_2FUM acid molecules is present in the network (Fig. 3b). The combination of these H-bonds arrangement gives rise to a 2D-sheet through the C–H···O H-bonds (see Table 2) derived from *methoxy*- and *acetate*- groups (Fig. 3c). The topology representation of the structure (Figure S7) shows that the crystal packing consists of a 2-nodal net, (2,4)-connected system and can be described with a point symbol $(\mathbf{8^4.12^2).(8)_2}$ with the vertices formed by the DIL^+ cation and H_2FUM acid acting as a bridge with the FUM^{2-}

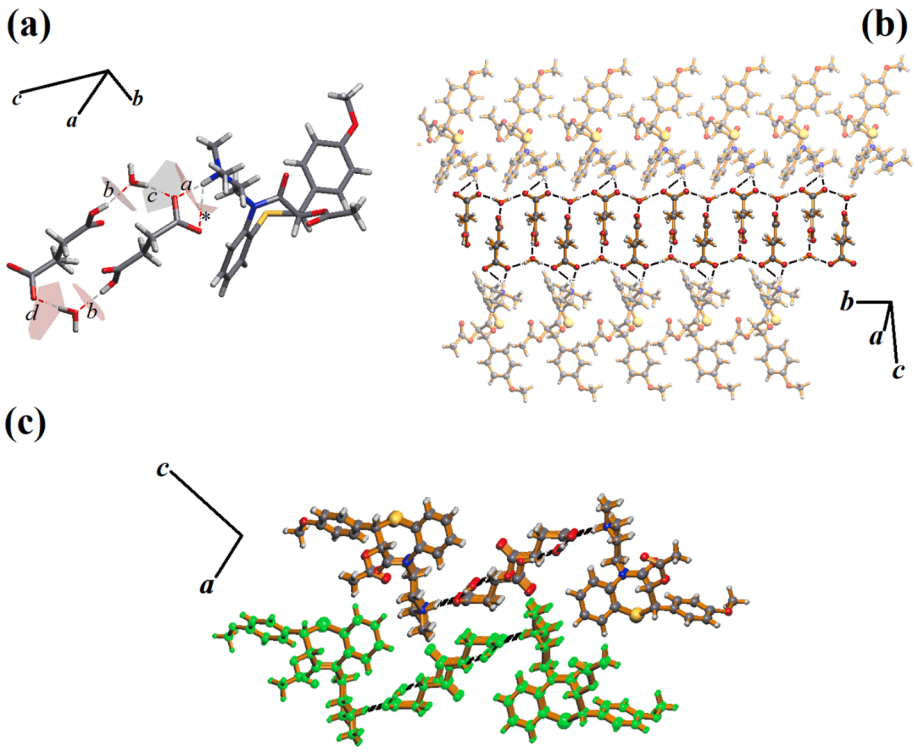

Fig. 1. (a) H-bonds view between DIL^+ cation, $HSUC^-$ anion, and water molecules. (b) $HSUC^-$ anion chain formation along the *b*-axis. (c) DIL-SUC-H_2O partial crystal packing at *ac*-plane. H-bonds are represented by dashed lines.

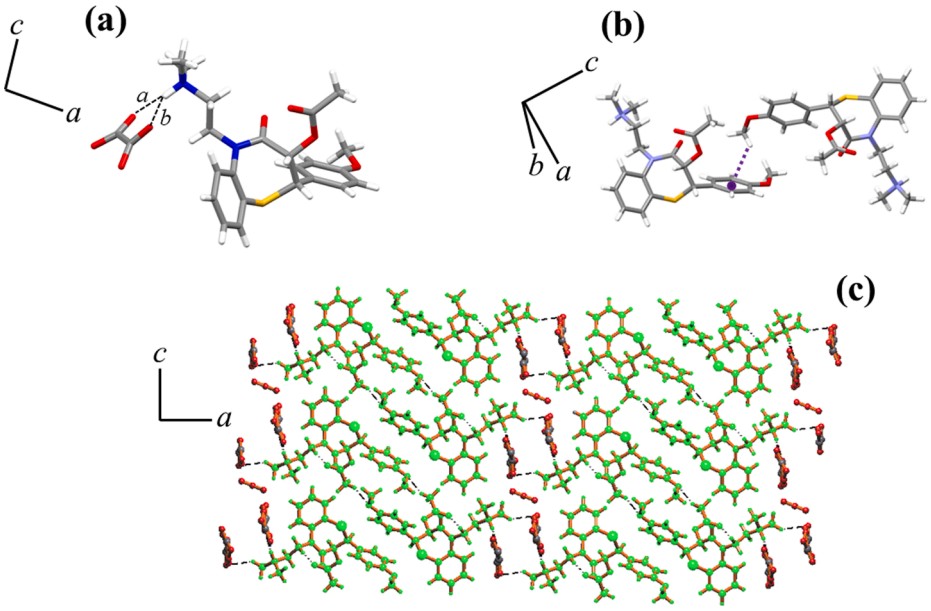

Fig. 2. (a) Bifurcated H-bonds in the DIL^+/$HOXA^-$ ionic pair. (b) C—H···π interaction between adjacent DIL^+ cations. (c) Representation of the columnar arrangement at *ac*-plane of the DIL-OXA-H_2O crystal packing. H-bonds are represented by dashed lines.

anions. Unlike the other two hydrated salts presented, the DIL-FUM-H_2FUM crystal packing is not columnar, which indeed influences the solubilization and dissolution processes of the API.

3.2. Hirshfeld surface analysis and energy framework studies

Molecular Hirshfeld surface (HS) is an isosurface constructed based on the partition of electronic distribution, hence, it provides a map of atom···atom contacts between molecules in the crystal environment (McKinnon et al., 2004). Fig. 4 shows the d_{norm} surface and their derived 2D-fingerprint plots of the DIL^+ cations from the reported salts. It is noted that the red spots represent the closest contacts on the N-atoms involved in CAHBs with the COO^- group of the corresponding anions. On the DIL^+ cation surface from DIL-OXA-H_2O and DIL-FUM-H_2FUM salts, these regions are spread than on the DIL-SUC-H_2O one because of bifurcated CAHBs between cation and anion. Furthermore, red spots can be observed on the C19 and C22 atoms from the *dimethylaminoethyl* fragments, being related to short C–H···O interactions that occurred

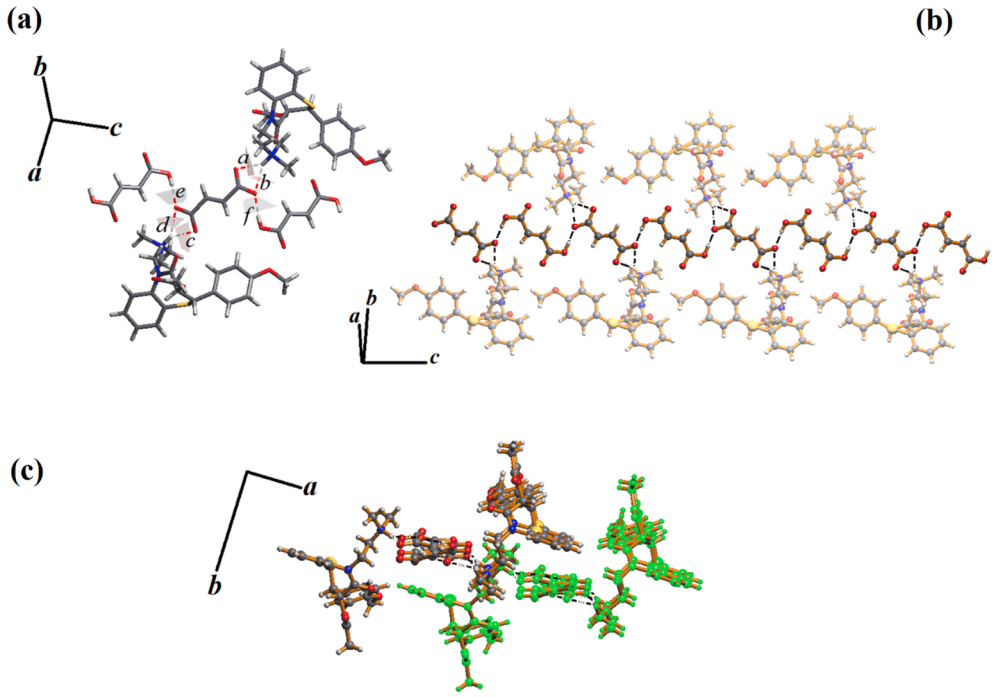

Fig. 3. (a) H-bonds representation between the DIL^+ cations (A and B), FUM^{2-} anion, and H_2FUM acid. (b) 1D-dimensional FUM^{2-}/H_2FUM chain that extends along the *c*-axis. (c) Partial crystal packing view of DIL-FUM-H_2FUM at *ab*-plane. H-bonds are represented by dashed lines.

between neighboring DIL^+ cations.

Based on the 2D-fingerprint plots derived from the HS, reasonable differences in the DIL^+ cations packing modes derived from each salt are noticed due to the distinct ionic pairs formed. First, we find that the spike assigned to H···O contacts with $d_e + d_i \approx 1.8$–1.9 Å is slightly more prominent in the DIL-SUC-H_2O diagram with minimal (d_i, d_e) combination of (0.6, 1.0) against (0.8, 1.1) for the oxalate and fumarate salts. Moreover, the 2D-fingerprint plot for the DIL-SUC-H_2O and DIL-OXA-H_2O salts show spread points near $di = de = 2.4$ while the DIL-FUM-H_2FUM salt-cocrystal, for being the densest compound, has a more compact 2D-fingerprint plot for both independent DIL^+ molecules. Also, a narrow light blue along the $di + de \approx 2.2$ Å diagonal - attributed to close H···H contacts - is more significant in the DIL-FUM-H_2FUM salt-cocrystal than other compounds. These differences in the 2D-plots demonstrate that the DIL^+ cation in the salt-cocrystal has experienced a slightly more crowded environment compared to other DIL salts.

The percentage contributions of intermolecular contacts of DIL^+ cations from the multicomponent crystals is presented in Figure S8. As expected, the largest contribution comes from the H···H contacts (ranging from 42.7 to 53.9%), followed by the O···H/H···O ones which are attributed to *X*−H···O H-bonds (where *X* = N, O, and C) formed between the DIL^+ cations and the respective anions. Interestingly, DIL-FUM-H_2FUM salt-cocrystal has one of the largest contributions of H···H contacts. Differently from the other salts evaluated, in its structure, the DIL^+ cations recognize each other by two C−H···π interactions. One occurs between *methoxyl* ring and *methoxyl-acetate* fragment and the other one involves *methoxyl* ring and C1-atom, resulting in a denser packing. For DIL-OXA-H_2O salt, its crystal packing presents the greatest contribution of O···H/H···O contacts among the reported salt forms. It can be explained by the fact that DIL^+ cation is associated with the $HOXA^-$ anion by its mean plane favoring stabilization by additional C−H···O interactions, and also motived by the conformation of the DIL^+ cation that leaves the *methoxyl* moiety available to interact. The DIL-FUM-H_2FUM salt-cocrystal, despite having an extra H_2FUM molecule, has a lower contribution of this contact compared to DIL-OXA-H_2O salt, since both coformers molecules display a not so favorable conformation to interact with DIL^+ cations. To better understand the structural similarities and differences between the new DIL crystal forms reported here and the already known DIL salt forms, an in-depth discussion has been inserted in the supplementary material (see also Figures S10–S20).

To access the energetic contribution of the supramolecular motifs, in terms of stabilizing interaction forces, toward understanding how packed the molecules are in the solid-state, energy framework studies have been also applied to visualize the relative magnitude and topology of the interaction energies (see Fig. 5 and Tables S12–S15). The crystal packings, except that of DIL-FUM-H_2FUM, are described as the stacking of 2D-sheet assemblies leading to the formation of columns. Thus, anions (Cl^-, $HSUC^-$, and $HOXA^-$) and water molecules are stabilized by both Coulombian (red) and dispersive (green) energies in the respective salt structures. The columnar arrangement of DIL^+ cations are sustained by these stabilizing interactions, resulting in an alternately triangular-shape energy topology (see Fig. 5a-c). Although the DIL-FUM-H_2FUM salt-cocrystal exhibits stabilizing energetic contributions similar to the other ones, the dispersive framework energy appears to play a more prominent role (cylinder thickness is slightly larger) for this form. Furthermore, the overall topology of the energy distributions for this compound has a distorted hexagonal-shape across the *ab*-plane (Fig. 5d). Therefore, it is expected that this another energy framework topology can play a more decisive role in drug solubilization and dissolution once it is evident that the polar domains are considerably less exposed on the salt-cocrystal structure.

Even though the correlation between interaction energy framework and physicochemical properties of APIs is not trivial, our results suggest important considerations. In terms of energy, the pairwise interaction energy between the DIL^+ cations and anions molecules as well as between adjacent DIL^+ molecules in the crystal lattices are not necessarily in the same magnitude. While the pairwise interaction energy between DIL^+ cations and anions ranged from −12.1 to −48.9 kJ mol^{-1}, the pairwise interaction energy between adjacent DIL^+ molecules ranged from −20.2 to −84.6 kJ mol^{-1} in the crystal structures (see Tables S12–S15). On the other hand, when we compared the cumulative framework energy considering a single unit cell and then we divide by the unit cell volume (in $Å^3$), it is noted that the DIL-HCl salt has the highest value (-0.415 kJ mol^{-1} $Å^{-3}$) followed by the DIL-FUM-H_2FUM

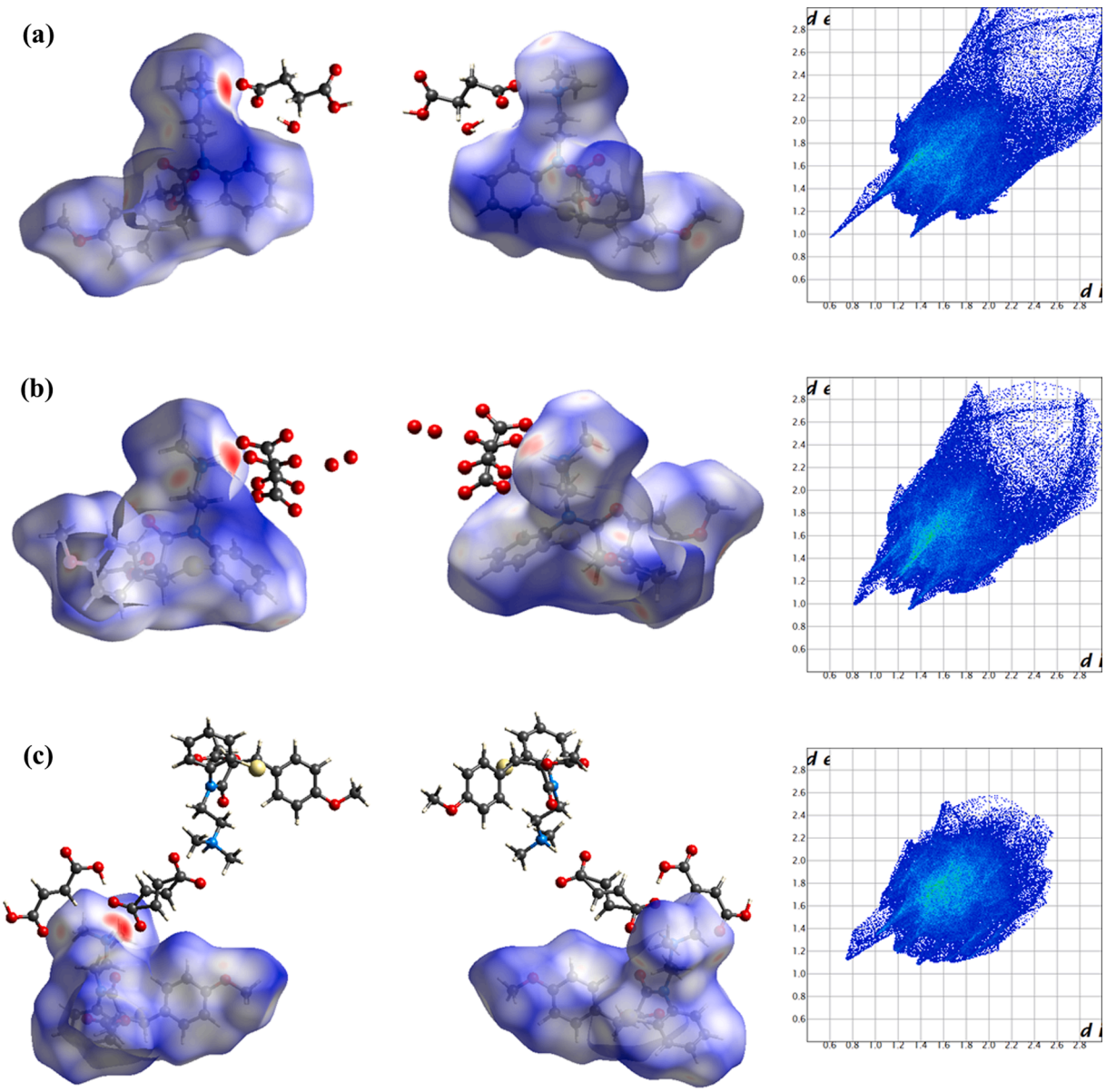

Fig. 4. Hirshfeld surfaces and 2D-fingerprint plots for the compounds: (a) DIL-SUC-H_2O, (b) DIL-OXA-H_2O, and (c) DIL-FUM-H_2FUM.

salt-cocrystal (-0.398 kJ mol^{-1} $Å^{-3}$). Despite these findings are consistent with the highest melting point values found for these compounds (see section 3.3.3), their solubilities exhibit opposite values (Table 3), which is somewhat intriguing. For the DIL-SUC-H_2O and DIL-OXA-H_2O salts, however, a reasonable correlation could be established since these forms present lower melting points and intermediate solubility values compared to the other compounds. This assumption is likely associated with the lowest total framework energy of the unit cell found for these salts (-0.229 kJ mol^{-1} $Å^{-3}$ for DIL-SUC-H_2O and −0.328 kJ mol^{-1} $Å^{-3}$ for DIL-OXA-H_2O). It is noteworthy that all these observations only point to a trend between crystal energy framework and physicochemical properties for this particular API.

3.3. Complementary Solid-State characterization

Further to the detailed crystallographic/topological and energy framework analyzes, the new DIL solid forms also experienced a comprehensive solid-state characterization through powder X-ray diffraction, infrared spectroscopy, and thermal techniques.

3.3.1. Powder X-ray diffraction

Powder X-ray diffraction experiments were conducted to establish the completeness concerning the DIL multicomponent crystals formation from the crystallization procedures. It is highly recommended to perform a PXRD analysis to check if the single-crystal chosen for the SCXRD data collection is representative of the whole sample. When we observe that the main Bragg peaks in the experimental PXRD pattern change their original 2θ positions compared to those observed for starting materials, it indicates that a new crystalline phase has been formed. As shown in Fig. 6, the experimental diffractograms of the three DIL solid forms are entirely different from those of the DIL-HCl commercial form and DIL free base. Moreover, the new solid forms derived from DIL display experimental PXRD patterns in excellent agreement with the simulated one, calculated from the final *CIF* files of each refinement. Due to DIL-OXA-H_2O crystalline nature, the non-corresponding peak at approximately 6° observed in its experimental diffractogram suggests that a potential crystalline phase, possibly a dehydrated form of DIL-OXA-H_2O, may have been formed by drying or storing this salt. Despite that, all observations from PXRD analyses have confirmed that the single-crystals obtained correspond to pure and

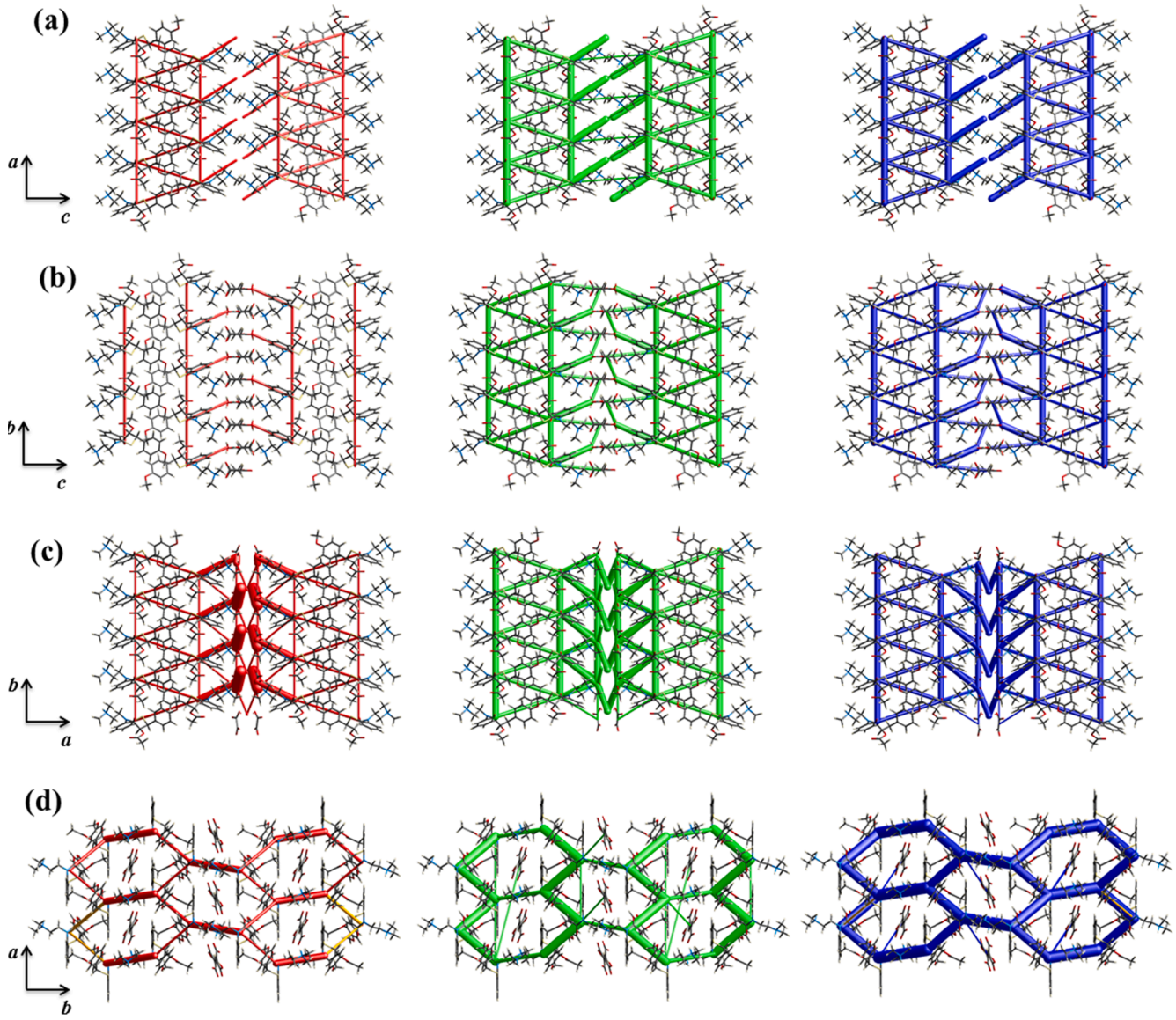

Fig. 5. Energy frameworks partitioned into electrostatic (red), dispersion (green) and total (blue) energetic components for the compounds: (a) DIL-HCl, (b) DIL-SUC-H_2O, (c) DIL-OXA-H_2O and (d) DIL-FUM-H_2FUM. The energy scale factor (tube size) is 100 and the energy threshold is 10 kJ mol^{-1}.

Table 3
Main physicochemical and pharmaceutical data of DIL-HCl, DIL-SUC-H_2O, DIL-OXA-H_2O and DIL-FUM-H_2FUM.

Compound	Melting point (°C)	Melting enthalpy (J g^{-1})	Decomposition temperature (°C)	Total framework energy *per* $Å^3$ (KJ mol^{-1})	Water solubility (mg mL^{-1})	IDR (mg cm^{-2} min^{-1})
DIL-HCl	213.9	−91.54	220	−0.415	565.13	15.68
DIL-SUC-H_2O	70.6	−188.96	180	−0.229	348.07	8.41
DIL-OXA-H_2O	112.1	−43.09	196	−0.328	382.71	9.65
DIL-FUM-H_2FUM	194.2	−95.59	202	−0.398	34.25	1.14

unique crystalline phases, being representative of the entire synthesized sample. The formation of possible hydrates derived from the DIL molecule can also be discarded.

3.3.2. *Infrared spectra*

Infrared spectroscopy was crucial to ratify the proton transfer and, hence, the final position of the hydrogen atoms on the structures. Furthermore, by providing information on the molecular vibrational modes (Heinz et al., 2009), this technique was additionally employed to identify the new DIL crystal forms. FT-IR spectra of DIL free base and their multicomponent systems are shown in Figure S9. Band assignments (see Table S16), as well as spectra interpretation, were carried out based on the crystal structures and using as reference spectroscopic data available for related DIL crystal forms (Shafi et al., 2017; Stepanovs et al., 2016). The main functional groups on the DIL molecule are ester, amide, and ether. In the DIL freebase spectrum, these groups display characteristics IR stretching frequencies at 1745 cm^{-1} (ester C=O stretch), 1673 cm^{-1} (amide C=O stretch), and 1060 and 1026 cm^{-1} (ether C−O stretches). Salt/cocrystal formations have been confirmed since these vibrational modes of drug molecule were also observed in the

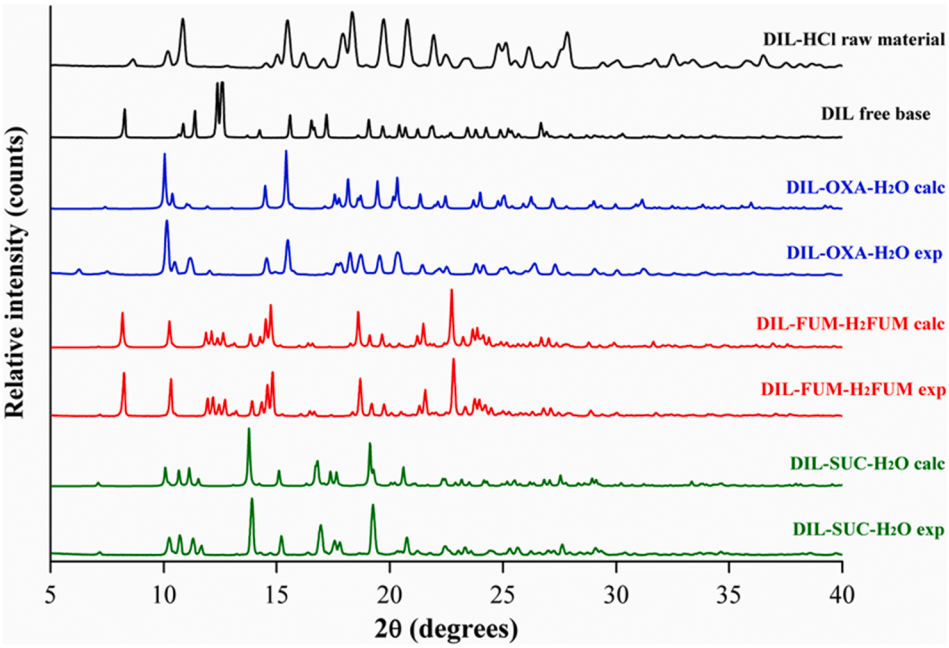

Fig. 6. Calculated (calc) and experimental (exp) PXRD patterns of DIL-HCl, DIL free base and, its new multicomponent solid forms.

salt spectra and further because it is noted the appearance of bands related to the dicarboxylic acids (coformers).

As mentioned, absorption bands appearing at ~1710 cm^{-1} characterize the salt and salt-cocrystal spectra. These bands have been assigned to the acid C=O stretching modes of partial deprotonated (succinate and oxalate) and fully protonated (fumaric acid) coformers molecules. Moreover, the FT-IR spectra of the new solid forms also exhibit new bands ranged from 1583 to 1410 cm^{-1}, which were attributed to the carboxylate antisymmetric and symmetric stretching modes, confirming the presence of the COO^{-} salt-forming group on the coformers

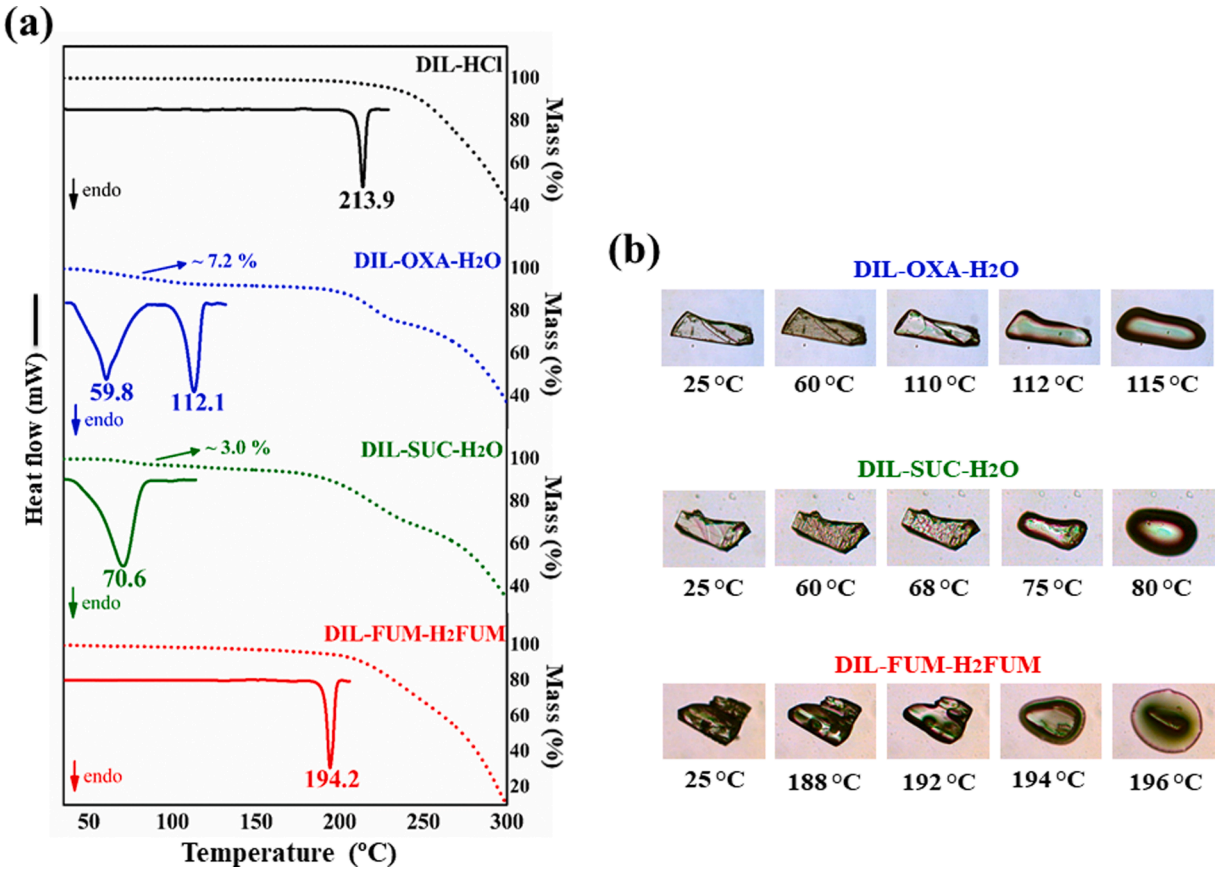

Fig. 7. (a) DSC curves (solid line) and TG thermograms (dashed line) and (b) hot stage microphotography for single-crystals of DIL and its new multicomponent solid forms.

molecules. All these observations are in agreement with the crystallographic analysis, which had previously shown not only the proton transfer but also real H-atoms positions on both DIL tertiary amine moiety and coformer carboxylic group.

3.3.3. Thermal analysis

The thermal profile of the DIL crystal forms was assessed by a combination of DSC, TG, and HSM analyses, as depicted in Fig. 7. DSC and TG plots of DIL-HCl were included for comparative purposes. The DIL-HCl salt is thermally stable up to 220 °C and its DSC curve exhibits a single endothermic melting peak at 213.9 °C (T_{onset} = 211.5 °C, ΔH = 91.54 J g^{-1}). The DIL-OXA-H_2O DSC curve, in turn, is characterized by two endothermic peaks at 59.8 °C (T_{onset} = 43.27 °C, ΔH = -72.53 J g^{-1}) and 112.1 °C (T_{onset} = 105.98 °C, ΔH = -43.03 J g^{-1}) that correspond to the dehydration and melting processes of the sample, respectively. These events are followed by a mass loss of ~ 7.2% in the wide temperature range of 40–110 °C in the TG curve, being consistent with the release of two structural water molecules and in agreement with the theoretical value (7.0%). Since water molecules on this dihydrate salt are trapped and interacting weakly *via* H-bonding in channels, dehydration, in this case, could occur without crystal structure rupture, which suggests the formation of its dehydrated form.

When we assessed the DSC curve of DIL-SUC-H_2O, we noticed the presence of only one endothermic peak centered at 70.6 °C (T_{onset} = 54.28 °C, ΔH = -182.57 J g^{-1}) that was assigned, at first, as a typical dehydration event. Nevertheless, the HSM photomicrographs (Fig. 7b) revealed that this salt starts to melt simultaneously with its dehydration. This unexpected behavior makes the DIL-SUC-H_2O compound an ionic liquid (IL), *i.e.,* an organic salt with a melting point below 100 °C (Stoimenovski et al., 2010). It is noteworthy that both events mentioned are accompanied by an initial mass loss of about 3.0% in the range of 50–100 °C in the TG curve, agreeing with the theoretical value of 3.2% that corresponds to the loss of one water molecule from the crystalline lattice. On the other hand, the DIL-FUM-H_2FUM thermal profile is similar to that observed for DIL-HCl since the DSC plot of the salt-cocrystal is also characterized by a single endothermic melting peak at 194.2 °C (T_{onset} = 191.76 °C, ΔH = -95.59 J g^{-1}) and its TG thermogram shows that this form is thermally stable up to ~202 °C. After this temperature, a gradual mass loss can be observed in the TG curve.

According to the TG data, all thermal events in the DSC curves have been assigned to dehydration or melting of the samples since they were not accompanied by a significant weight loss step in the corresponding TG thermograms. Based on the decomposition/melting temperatures of each compound (see Table 3) and further considering that both melting, and degradation processes require the rupture of the crystal structure, the following thermal stability order can be established: DIL-HCl > DIL-FUM-H_2FUM > DIL-OXA-H_2O > DIL-SUC-H_2O. Finally, HSM experiments successfully confirmed the DSC/TG result interpretations. In the HSM photomicrographs (Fig. 7b), it is possible to note the beginning of the crystals melting of the DIL-OXA-H_2O (~112 °C), DIL-SUC-H_2O (~75 °C), and DIL-FUM-H_2FUM (~194 °C). Also, for both oxalate and succinate hydrated salts we observe the darkening of the DIL-OXA-H_2O and DIL-SUC-H_2O crystals at approximately 60 °C due to their dehydration processes.

3.4. Pharmaceutical implications

As previously mentioned, the ready solubilization and dissolution of the DIL are harmful to drug pharmacokinetics. Thus, after the in-deep structural characterization of the new crystal solid forms, it is claimed to verify their efficiency in optimizing the drug solubility and dissolution processes.

3.4.1. Equilibrium solubility

Solubility is regarded as the main biopharmaceutical attribute of an API since it has an immense impact on the drug bioavailability and, hence, on its pharmacological response (Williams et al., 2013). Apart from that, crystal engineering is a well-consolidated approach to optimize this property, especially for ionizable APIs. For DIL, which presents short elimination half-life due to high solubility, the synthesis of less soluble crystal forms is a central requirement for future extended-release formulations. The equilibrium solubility of DIL-HCl and its new solid forms in buffered media that mimic physiological conditions is presented in Fig. 8. Overall, even though the DIL-OXA-H_2O and DIL-SUC-H_2O salts have high solubility values, being even close to the ones found for the DIL-HCl, the DIL-FUM-H_2FUM salt-cocrystal, in turn, showed a substantial decrease in its solubility, corroborating our expectations. It is worth mentioning that all compounds submitted to the solubility and intrinsic dissolution tests were found to be stable at the end of the experiments. The final pH values, measured after the solubility studies, did not show any significant variation (Table S17). Besides that, the FT-IR data showed that the crystal structure of the solid residues and the undissolved disks obtained after the solubility and dissolution experiments, respectively, remain the same that the original ones (data not shown), excluding even the formation of hydrates.

First, the DIL-HCl solubility in all dissolution media is in accordance with the values found in the literature (Sood and Panchagnula, 1998). As already mentioned, the hydrochloride form proved to be very soluble, with values ranging from 545.01 ± 28.48 to 565.13 ± 9.96 mg mL^{-1}. Similarly, both oxalate and succinate hydrated salts also showed high solubility values in all dissolution media. For these salts, for instance, the solubility in purified water was 382.71 ± 3.85 mg mL^{-1} (DIL-OXA-H_2O) and 348.07 ± 31.60 mg mL^{-1} (DIL-SUC-H_2O), being slightly lower (from 1.6 to 1.5-folds) than the DIL-HCl commercial form. In contrast, the solubility of DIL-FUM-H_2FUM salt-cocrystal, for being the compound with a more dense and cohesive crystal packing, is considerably lower in the four dissolution media (Fig. 8) compared to the other three DIL salts. Significant solubility decreases ranged from 12.5 to 21.4-fold were observed. From a structural point of view, these results can be attributed, in part, to the supramolecular architectures of the compounds. In the DIL salts, their crystal packings are dominated by hydrophilic regions, *i.e.,* molecular channel subsets, where the anions/water molecules, as well as the polar functional groups, are arranged. Apparently, these crystal packing assemblies play a crucial role in the prompt API solubilization.

3.4.2. Intrinsic dissolution and dissolution profile

Dissolution studies are complementary to those of solubility, being crucial in understanding how the solid-state form dictates the drug release rate (Siepmann and Siepmann, 2013). In order to investigate as the new solid forms affected the dissolution behaviors, their intrinsic dissolution rates (IDRs) and powder dissolution profiles have been determined. All organic salts reported herein present lower IDRs values compared to DIL-HCl (see Table 3). The DIL-OXA-H_2O (9.65 ± 1.51 mg cm^{-2} min^{-1}) and DIL-SUC-H_2O (8.41 ± 0.94 mg cm^{-2} min^{-1}) exhibited a 1.6 and 1.9-fold slower dissolution rate, respectively, compared to DIL-HCl (15.68 ± 2.45 mg cm^{-2} min^{-1}). Nevertheless, the dissolution rate of the DIL-FUM-H_2FUM is found to be about 13.7 (1.14 ± 0.34 mg cm^{-2} min^{-1}) times lower than that of DIL-HCl, confirming that the cocrystallization of DIL with fumaric acid has a remarkable influence on the intrinsic dissolution rate of the API, as illustrated in Fig. 9a. This behavior is expected from structures containing molecules efficiently packaged that, when exposed to an aqueous medium, hinders the rupture of the crystal structures by water molecules on the dissolution process.

Meanwhile, it is noted that the dissolution profiles are quite similar to each other (Fig. 9b). All compounds tested reached the concentration referring to plateau, *i.e.,* 100% of drug release, approximately within 7 min after inserting the capsules in the dissolution vessels. Even though we succeeded in decreasing the solubility of the drug and its intrinsic dissolution rate, the dissolution profile results suggest that the relatively high solubility of the DIL crystal forms has made the capsule formulation

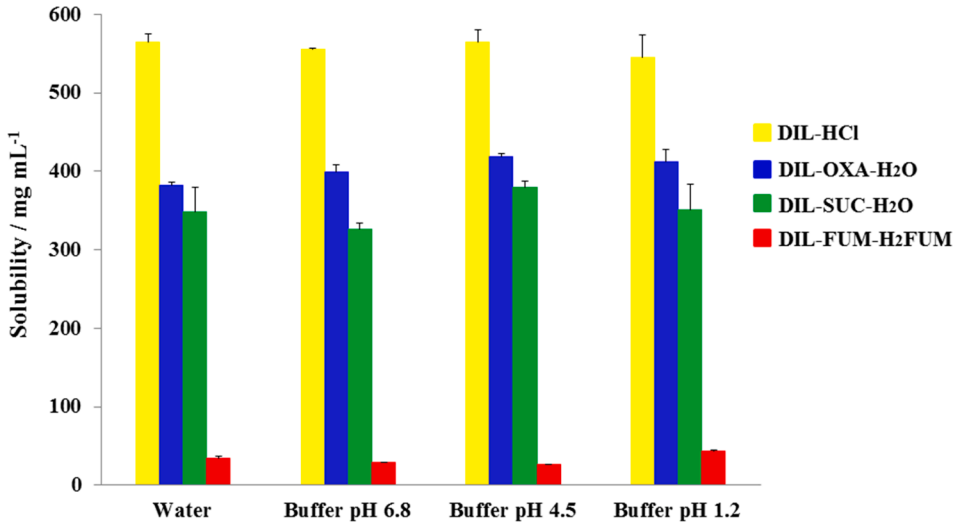

Fig. 8. Solubility values (mg mL^{-1}) founded for DIL-HCl and its new multicomponent solid forms in different dissolution media.

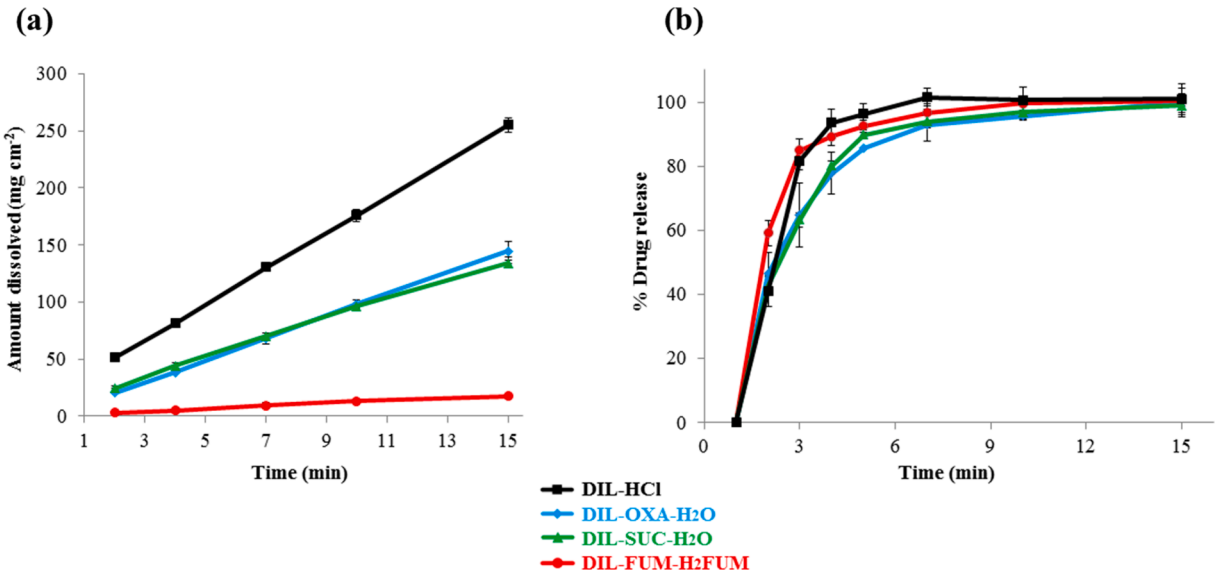

Fig. 9. (a) Intrinsic dissolution plots and (b) dissolution profiles of DIL-HCl and its new multicomponent solid forms in water.

strategy unable to retard the DIL release. This was expected to occur for a biopharmaceutical classification system (BCS) class I drug such as DIL. In this particular case, the sustained drug-releasing from the modified crystals would become noticeable through the addition of excipients, in the formulation, known for slow up the drug delivery, beyond a more appropriate solid oral dosage form, instead of capsules. Based on the premise that slow-release preparations of DIL require crystal forms of slower dissolving and less soluble, the present investigation has fulfilled its goal.

Given these results, the following solubility/IDR order can be established for DIL solid forms: DIL-HCl > DIL-OXA-H_2O ≅ DIL-SUC-H_2O > DIL-FUM-H_2FUM. A general observation involving these new crystals derived from DIL was that the compound with the highest energy framework density (DIL-FUM-H_2FUM) was also the one that had the lowest solubility and IDR values. By correlating the solubility/dissolution data with structural and energy framework attributes, we hypothesize that the columnar 3D-assemblies formed by the hydrochloride, succinate, and oxalate salts, indeed, contribute to the DIL dissolution and solubilization. Also, the same energy distribution topologies (triangular shapes), as well as the lower energy framework densities (except for the DIL-HCl salt), corroborate our conjecture. On the other hand, the DIL-FUM-H_2FUM salt-cocrystal proved to be the less soluble form and with the lowest IDR, suggesting that the fumarate/fumaric acid chain that is surrounded by DIL^+ cations molecules in its 3D-crystal arrangement not only generates a hexagonal-shape energy framework topology but also seem to hamper DIL dissolution and solubilization from the crystal. Unlike the other three DIL salts, in the DIL-FUM-H_2FUM structure, the polar domains of the molecules are less exposed in the crystal, which further inhibits the degree of solvation of drug molecules during both solubility and dissolution processes.

Regarding the possible impacts of the crystal forms on the pharmacokinetic of DIL, even though no *in vivo* experimental evidence about drug elimination half-life optimization has been provided, the results presented here are suggestive that the new salt/cocrystal forms may improve the short elimination half-life of DIL and even its other pharmacokinetic parameters. Being a BCS drug class I and assuming that the drug permeability would not be significantly modified only by coformer/counter-ion changing, the absorption would become sensitive to the solubility and, mainly, the dissolution rate. Thus, by changing the absorption process, a direct impact would be noted on maximum serum

concentration and elimination half-life of the API. Although this process *in vivo* is not straightforward, there is enough evidence to support that short half-life drugs could be improved, based on these assumptions (Sugano and Terada, 2015; Wen et al., 2015). Thus, by simultaneously promoting the reduction of both solubility and dissolution rate of DIL, we hypothesized that future slow-release pharmaceutical formulations containing these new crystals could, indeed, affect the elimination half-life of DIL, for the reasons mentioned.

4. Conclusions

Three multicomponent ionic crystals of the antihypertensive drug DIL, being two hydrated salts (DIL-SUC-H_2O and DIL-OXA-H_2O) and one salt-cocrystal (DIL-FUM-H_2FUM) have been successfully prepared from reactions of DIL free base with pharmaceutically acceptable dicarboxylic acids (succinic, oxalic, and fumaric). These crystal modifications were engineered aiming to reduce the solubility and dissolution rate of DIL. From the structural elucidation by SCXRD we concluded that the DIL^+ cations exhibited an expected twisted-boat conformation, being further stabilized by robust H-bonds that mainly involve the COO^- and protonated tertiary amine groups. Also, 2D-sheet assemblies stabilized by both classical (N–H···O, O–H···O) and non-classical (C–H···O) H-bonds are observed in all crystal networks. It noteworthy that the crystallographic and energy framework descriptions revealed not only the energy densities of each unit cell but also the distinct energy distribution topologies generated from the stabilizing interactions. From a pharmaceutical point of view, in the solubility and intrinsic dissolution tests, the values found have demonstrated a meaningful decrease of these properties, especially for the DIL-FUM-H_2FUM salt-cocrystal that proved to be 16.5 times less soluble and with a dissolution rate 13.7 times slower compared to DIL-HCl. Therefore, our investigation implies that the cocrystallization of the antihypertensive drug diltiazem with fumaric acid offers one of the central requirements concerning the use of this API in future pharmaceutical formulations of modified release.

CRediT authorship contribution statement

Luan F. Diniz: Conceptualization, Investigation, Methodology, Formal analysis, Writing - original draft, Writing - review & editing. **Chris H.J. Franco:** Formal analysis, Writing - original draft. **Daniely F. Silva:** Methodology, Visualization. **Larissa S. Martins:** Methodology, Visualization. **Paulo S. Carvalho Jr:** Methodology, Writing - review & editing. **Mateus A.C. Souza:** Methodology, Data curation, Visualization. **Naialy F.A. Reis:** . **Christian Fernandes:** Conceptualization, Investigation, Writing - review & editing, Supervision, Funding acquisition. **Renata Diniz:** Investigation, Visualization, Writing - review & editing, Supervision, Project administration, Funding acquisition.

Declaration of Competing Interest

The authors declare that they have no known competing financial interests or personal relationships that could have appeared to influence the work reported in this paper.

Acknowledgments

The authors acknowledge the Brazilian funding agencies CAPES, FAPEMIG, and CNPq (311725/2020-1 and 420052/2018-6) for financial support. We also thank Dra. Mara Irene Yoshida (DQ/UFMG) by both DSC/TG measurements and Laboratório Multi-usuário de Cristalografia Estrutural (LaMuCrEs - IFSC/USP) for providing HSM analyzes. The authors would like to thank Dra. Charlane Cimini Correa (DQ/UFJF) for allowing access to the SCXRD facilities. Finally, we deeply appreciate Dr. Rubén Dario Sinisterra and Dr. Lucius F. O. Bomfim Filho (DQ/UFMG) for their help in the intrinsic dissolution analyzes.

Appendix A. Supplementary data

Supplementary data to this article can be found online at https://doi.org/10.1016/j.ijpharm.2021.120790.

References

Almansa, C., Merce, R., Tesson, N., Farran, J., Tomàs, J., Plata-Salaman, C.R., 2017. Co-Crystal of Tramadol hydrochloride–Celecoxib (CTC): a novel API–API co-crystal for the treatment of pain. Cryst. Growth Des. 17, 1884–1892. https://doi.org/10.1021/acs.cgd.6b01848.

Berry, D.J., Steed, J.W., 2017. Pharmaceutical cocrystals, salts and multicomponent systems; intermolecular interactions and property based design. Adv. Drug Deliv. Rev. 117, 3–24. https://doi.org/10.1016/j.addr.2017.03.003.

Blagden, N., de Matas, M., Gavan, P.T., York, P., 2007. Crystal engineering of active pharmaceutical ingredients to improve solubility and dissolution rates. Adv. Drug Deliv. Rev. 59 (7), 617–630. https://doi.org/10.1016/j.addr.2007.05.011.

Blatov, V.A., Shevchenko, A.P., Proserpio, D.M., 2014. Applied Topological Analysis of Crystal Structures with the Program Package ToposPro. Cryst. Growth Des. 14 (7), 3576–3586. https://doi.org/10.1021/cg500498k.

Cheney, M.L., Shan, N., Healey, E.R., Hanna, M., Wojtas, L., Zaworotko, M.J., Sava, V., Song, S., Sanchez-Ramos, J.R., 2010. Effects of crystal form on solubility and pharmacokinetics: a crystal engineering case study of lamotrigine. Cryst. Growth Des. 10 (1), 394–405. https://doi.org/10.1021/cg901010v.

Childs, S.L., Stahly, G.P., Park, A., 2007. The salt-cocrystal continuum: The influence of crystal structure on ionization state. Mol. Pharm. 4, 323–338. https://doi.org/10.1021/mp0601345.

Cruz-Cabeza, A.J., 2012. Acid–base crystalline complexes and the pKa rule. CrystEngComm 14 (20), 6362. https://doi.org/10.1039/c2ce26055g.

Desiraju, G.R., 2013. Crystal engineering: From molecule to crystal. J. Am. Chem. Soc. 135 (27), 9952–9967. https://doi.org/10.1021/ja403264c.

Dolomanov, O.V., Bourhis, L.J., Gildea, R.J., Howard, J.A.K., Puschmann, H., 2009. OLEX2: A complete structure solution, refinement and analysis program. J. Appl. Crystallogr. 42 (2), 339–341. https://doi.org/10.1107/S0021889808042726.

Duggirala, N.K., Perry, M.L., Almarsson, Ö., Zaworotko, M.J., 2016. Pharmaceutical cocrystals: along the path to improved medicines. Chem. Commun. 52 (4), 640–655. https://doi.org/10.1039/C5CC08216A.

Elder, D.P., Holm, R., Diego, H.L.d., 2013. Use of pharmaceutical salts and cocrystals to address the issue of poor solubility. Int. J. Pharm. 453 (1), 88–100. https://doi.org/10.1016/j.ijpharm.2012.11.028.

Farhana, S.A., Shantakumar, S.M., Narasu, L., 2009. Sustained release of diltiazem hydrochloride from chitosan micro-capsules. Curr. Drug Deliv. 6, 238–248. https://doi.org/10.2174/156720109788680840.

Farrugia, L.J., 2012. WinGX and ORTEP for Windows: An update. J. Appl. Crystallogr. 45 (4), 849–854. https://doi.org/10.1107/S0021889812029111.

Flack, H.D., Bernardinelli, G., 1999. Absolute structure and absolute configuration. Acta Crystallogr. Sect. A Found. Crystallogr. 55 (5), 908–915. https://doi.org/10.1107/S0108767399004262.

Gadade, D.D., Pekamwar, S.S., 2016. Pharmaceutical Cocrystals: Regulatory and Strategic Aspects, Design and Development. Adv. Pharm. Bull. 6, 479–494. https://doi.org/10.15171/apb.2016.062.

Gascon, N., Almansa, C., Merlos, M., Miguel Vela, J., Encina, G., Morte, A., Smith, K., Plata-Salamán, C., 2019. Co-crystal of tramadol-celecoxib: preclinical and clinical evaluation of a novel analgesic. Expert. Opin Inv. Drug. 28 (5), 399–409. https://doi.org/10.1080/13543784.2019.1612557.

Glomme, A., März, J., Dressman, J.B., 2005. Comparison of a miniaturized shake-flask solubility method with automated potentiometric acid/base titrations and calculated solubilities. J. Pharm. Sci. 94 (1), 1–16. https://doi.org/10.1002/jps.20212.

Grell, J., Bernstein, J., Tinhofer, G., 1999. Graph-set analysis of hydrogen-bond patterns: some mathematical concepts. Acta Crystallogr. Sect. B 55 (6), 1030–1043. https://doi.org/10.1107/S0108768199007120.

Groom, C.R., Bruno, I.J., Lightfoot, M.P., Ward, S.C., 2016. The Cambridge structural database. Acta Crystallogr. Sect. B Struct. Sci. Cryst. Eng. Mater. 72, 171–179. https://doi.org/10.1107/S2052520616003954.

Grothe, E., Meekes, H., Vlieg, E., ter Horst, J.H., de Gelder, R., 2016. Solvates, Salts, and Cocrystals: A Proposal for a Feasible Classification System. Cryst. Growth Des. 16 (6), 3237–3243. https://doi.org/10.1021/acs.cgd.6b00200.

Han, X., Wang, L., Sun, Y., Liu, X., Liu, W., Du, Y., Li, L., Sun, J., 2013. Preparation and evaluation of sustained-release diltiazem hydrochloride pellets. Asian J. Pharm. Sci. 8 (4), 244–251. https://doi.org/10.1016/j.ajps.2013.09.007.

Heinz, A., Strachan, C.J., Gordon, K.C., Rades, T., 2009. Analysis of solid-state transformations of pharmaceutical compounds using vibrational spectroscopy. J. Pharm. Pharmacol. 61 (8), 971–988. https://doi.org/10.1211/jpp/61.08.0001.

Hermann, P.h., Rodger, S.D., Remones, G., Thenot, J.P., London, D.R., Morselli, P.L., 1983. Pharmacokinetics of diltiazem after intravenous and oral administration. Eur. J. Clin. Pharmacol. 24 (3), 349–352. https://doi.org/10.1007/BF00610053.

ICH, 2005. ICH Topic Q2 (R1) Validation of Analytical Procedures : Text and Methodology, International Conference on Harmonisation of Technical Requirements for Registration of Pharmaceuticals for Human Use. Geneva. https://doi.org/http://www.ich.org/fileadmin/Public_Web_Site/ICH_Products/Guidelines/Quality/Q2_R1/Step4/Q2_R1__Guideline.pdf.

Kaialy, W., Bello, H., Asare-Addo, K., Nokhodchi, A., 2016. Effect of solvent on retarding the release of diltiazem HCl from Polyox-based liquisolid tablets. J. Pharm. Pharmacol. 68, 1396–1402. https://doi.org/10.1111/jphp.12643.

Karimi-Jafari, M., Padrela, L., Walker, G.M., Croker, D.M., 2018. Creating Cocrystals: A Review of Pharmaceutical Cocrystal Preparation Routes and Applications. Cryst. Growth Des. 18 (10), 6370–6387. https://doi.org/10.1021/acs.cgd.8b00933.

Kojić-Prodić, B., Ružić-Toroš, Ži, Šunjić, V., Decorte, E., Moimas, F., 1984. Absolute Conformation and Configuration of (2S, 3S)-3-Acetoxy-5-(dimethylaminoethyl)-2-(4-methoxyphenyl)-2,3-dihydro-1,5-benzothiazepin-4(5H)-one Chloride (Dilthiazem Hydrochloride). Helv. Chim. Acta 67 (3), 916–926. https://doi.org/10.1002/hlca.19840670333.

Kojima, H., Yoshihara, K., Sawada, T., Kondo, H., Sako, K., 2008. Extended release of a large amount of highly water-soluble diltiazem hydrochloride by utilizing counter polymer in polyethylene oxides (PEO)/polyethylene glycol (PEG) matrix tablets. Eur. J. Pharm. Biopharm. 70 (2), 556–562. https://doi.org/10.1016/j.ejpb.2008.05.032.

Kristmundsdóttir, T., Gudmundsson, Ó.S., Ingvarsdóttir, K., 1996. Release of diltiazem from Eudragit microparticles prepared by spray-drying. Int. J. Pharm. 137 (2), 159–165. https://doi.org/10.1016/0378-5173(96)04509-7.

Li, D., Kong, M., Li, J., Deng, Z., Zhang, H., 2018. Amine–carboxylate supramolecular synthon in pharmaceutical cocrystals. CrystEngComm 20 (35), 5112–5118. https://doi.org/10.1039/C8CE01106K.

Mackenzie, C.F., Spackman, P.R., Jayatilaka, D., Spackman, M.A., 2017. CrystalExplorer model energies and energy frameworks: extension to metal coordination compounds, organic salts, solvates and open-shell systems. IUCrJ 4 (5), 575–587. https://doi.org/10.1107/S205225251700848X.

Macrae, C.F., Sovago, I., Cottrell, S.J., Galek, P.T.A., McCabe, P., Pidcock, E., Platings, M., Shields, G.P., Stevens, J.S., Towler, M., Wood, P.A., 2020. Mercury 4.0: From visualization to analysis, design and prediction. J. Appl. Crystallogr. 53, 226–235. https://doi.org/10.1107/S1600576719014092.

McKinnon, J.J., Spackman, M.A., Mitchell, A.S., 2004. Novel tools for visualizing and exploring intermolecular interactions in molecular crystals. Acta Crystallogr. Sect. B 60 (6), 627–668. https://doi.org/10.1107/S0108768104020300.

Motherwell, W.D.S., Shields, G.P., Allen, F.H., 2000. Graph-set and packing analysis of hydrogen-bonded networks in polyamide structures in the Cambridge Structural Database. Acta Crystallogr. Sect. B 56 (5), 857–871. https://doi.org/10.1107/S0108768100007230.

Rigaku Oxford Diffraction, 2014. CrysAlisPro Data Collection and Processing Software for Agilent X-ray Diffractometers. Technol, UK Ltd, Yarnton, Oxford, UK.

Schultheiss, N., Newman, A., 2009. Pharmaceutical cocrystals and their physicochemical properties. Cryst. Growth Des. https://doi.org/10.1021/cg900129f.

Serajuddin, A.T.M., 2007. Salt formation to improve drug solubility. Adv. Drug Deliv. Rev. https://doi.org/10.1016/j.addr.2007.05.010.

Shafi, N., Siddiqui, F.A., Arayne, M.S., Sultana, N., 2017. In-vitro drug–drug interaction studies of diltiazem with floroquinolones. J. Liq. Chromatogr. Relat. Technol. 40 (20), 1003–1014. https://doi.org/10.1080/10826076.2017.1386675.

Shan, N., Zaworotko, M.J., 2008. The role of cocrystals in pharmaceutical science. Drug Discov. Today 13 (9-10), 440–446. https://doi.org/10.1016/j.drudis.2008.03.004.

Sheldrick, G.M., 2015a. SHELXT - Integrated space-group and crystal-structure determination. Acta Crystallogr. Sect. A Found. Crystallogr. 71, 3–8. https://doi.org/10.1107/S2053273314026370.

Sheldrick, G.M., 2015b. Crystal structure refinement with SHELXL. Acta Crystallogr. Sect. C Struct. Chem. 71, 3–8. https://doi.org/10.1107/S2053229614024218.

Siepmann, J., Siepmann, F., 2013. Mathematical modeling of drug dissolution. Int. J. Pharm. 453 (1), 12–24. https://doi.org/10.1016/j.ijpharm.2013.04.044.

Sood, A., Panchagnula, R., 1998. Drug release evaluation of diltiazem CR preparations. Int. J. Pharm. 175, 95–107. https://doi.org/10.1016/S0378-5173(98)00268-3.

Spackman, M.A., Jayatilaka, D., 2009. Hirshfeld surface analysis. CrystEngComm 11 (1), 19–32. https://doi.org/10.1039/B818330A.

Steed, J.W., 2013. The role of co-crystals in pharmaceutical design. Trends Pharmacol. Sci. 34 (3), 185–193. https://doi.org/10.1016/j.tips.2012.12.003.

Stepanovs, D., Jure, M., Gosteva, M., Popelis, J., Kiselovs, G., Mishnev, A., 2016. Crystal structures and physicochemical properties of diltiazem base and its acetylsalicylate, nicotinate and L-malate salts. CrystEngComm 18, 1235–1241. https://doi.org/10.1039/C5CE01204J.

Stoimenovski, J., MacFarlane, D.R., Bica, K., Rogers, R.D., 2010. Crystalline vs. Ionic Liquid Salt Forms of Active Pharmaceutical Ingredients: A Position Paper. Pharm. Res. 27 (4), 521–526. https://doi.org/10.1007/s11095-009-0030-0.

Sugano, K., Terada, K., 2015. Rate-and extent-limiting factors of oral drug absorption: theory and applications. J. Pharm. Sci. 104 (9), 2777–2788. https://doi.org/10.1002/jps.24391.

Turner, M.J., McKinnon, J.J., Wolff, S.K., Grimwood, D.J., Spackman, P.R., Jayatilaka, D., Spackman, M.A., 2017. CrystalExplorer17. University of Western, Australia.

Turner, M.J., Thomas, S.P., Shi, M.W., Jayatilaka, D., Spackman, M.A., 2015. Energy frameworks: insights into interaction anisotropy and the mechanical properties of molecular crystals. Chem. Commun. 51 (18), 3735–3738. https://doi.org/10.1039/C4CC09074H.

Weir, M.R., 1995. Diltiazem: Ten Years of Clinical Experience in the Treatment of Hypertension. J. Clin. Pharmacol. 35, 220–232. https://doi.org/10.1002/j.1552-4604.1995.tb04051.x.

Wen, H., Jung, H., Li, X., 2015. Drug delivery approaches in addressing clinical pharmacology-related issues: opportunities and challenges. AAPS J. 17 (6), 1327–1340. https://doi.org/10.1208/s12248-015-9814-9.

Williams, H.D., Trevaskis, N.L., Charman, S.A., Shanker, R.M., Charman, W.N., Pouton, C.W., Porter, C.J.H., Christopoulos, A., 2013. Strategies to Address Low Drug Solubility in Discovery and Development. Pharmacol. Rev. 65 (1), 315–499. https://doi.org/10.1124/pr.112.005660.